Efficient Electrical Spin Readout of NV$^-$ Centers in Diamond

Florian M. Hrubesch,* Georg Braunbeck, Martin Stutzmann, Friedemann Reinhard,† and Martin S. Brandt‡
Walter Schottky Institut and Physik-Department, Technische Universität München, Am Coulombwall 4, 85748 Garching, Germany
(Received 5 September 2016; published 17 January 2017)

Using pulsed photoionization the coherent spin manipulation and echo formation of ensembles of NV$^-$ centers in diamond are detected electrically, realizing contrasts of up to 17%. The underlying spin-dependent ionization dynamics are investigated experimentally and compared to Monte Carlo simulations. This allows the identification of the conditions optimizing contrast and sensitivity, which compare favorably with respect to optical detection.

DOI: 10.1103/PhysRevLett.118.037601

With its long coherence time [1] and fluorescence detection [2], the NV$^-$ nitrogen vacancy center in diamond is a promising candidate for quantum applications. These features have enabled its use, e.g., as a sensor for magnetic fields [3,4] and temperature [5], for scanning-probe spin imaging [6], and structure determination [7]. However, optical spin readout has drawbacks: it is inefficient, requiring several hundred repetitions for a single spin readout, and often cumbersome. Electric spin readout appears attractive to surmount these limitations. It could enable access to NV$^-$ centers in dense arrays, with a spacing limited by the few-nanometer-small feature size of electron beam lithography [8]. It might, moreover, provide a way to read out other spin defects [9–11], potentially including optically inactive ones. Two methods for the electric readout of NV$^-$ centers have been demonstrated, based on nonradiative energy transfer to graphene [12] and direct photoionization of the NV$^-$ centers in the diamond host crystal (photocurrent detection of magnetic resonance [13]). Both methods, however, have until now only been used with continuous wave (cw) spin manipulation and have therefore remained limited to NV$^-$ detection. Here, we introduce a scheme based on both pulsed spin manipulation and pulsed photoionization to truly read out the spin state of NV$^-$ centers electrically after coherent control and demonstrate it on small ensembles. We employ this scheme to establish a quantitative model of photoionization, simulate the readout efficiency, and predict that under optimized conditions pulsed electric readout could outperform optical fluorescence detection.

The spin-dependent photoionization cycle can be understood as two two-photon processes, whose spin dependence relies on the NV$^-$ center's intersystem crossing (ISC) [Fig. 1(a)] [13]. A first photon (green arrows) triggers the shelving (black arrow) of NV$^-$ centers in spin state $|2\rangle$ (corresponding to the $m_S = \pm 1$ spin quantum numbers of the NV$^-$ center) into the long-lived metastable singlet state $|5\rangle$ by this ISC. Since shelving protects this state from further laser excitation, the absorption of a second photon preferentially ionizes NV$^-$ centers prepared in spin state $|1\rangle$ (corresponding to $m_S = 0$) into the conduction band, creating a spin-dependent photocurrent (blue arrow) proportional to the population of the $m_S = 0$ state. Microwave pulses (red arrow) increasing the $m_S = \pm 1$ population will then lead to a resonant reduction of the photocurrent. Two further photons recharge the NV^0 center into its negative charge state by excitation of the NV^0 center (photon 3) and capture of an electron (photon 4) from the valence band [14].

Our spin readout experiments are performed in a photoconductor [Fig. 1(b)]. We illuminate a densely N-doped diamond (Element Six, grown by chemical vapor deposition, [N] < 1 ppm, [NV] ≈10 ppb) with a green laser (wavelength 532 nm) pulse generated by a Nd:YAG laser and an acousto-optic modulator (AOM) and observe the resulting photocurrent between two interdigit Schottky contacts, biased with 5 V. The contacts (finger width 5 μm, finger-to-finger distance 10 μm) consist of a 10-nm-thick titanium and an

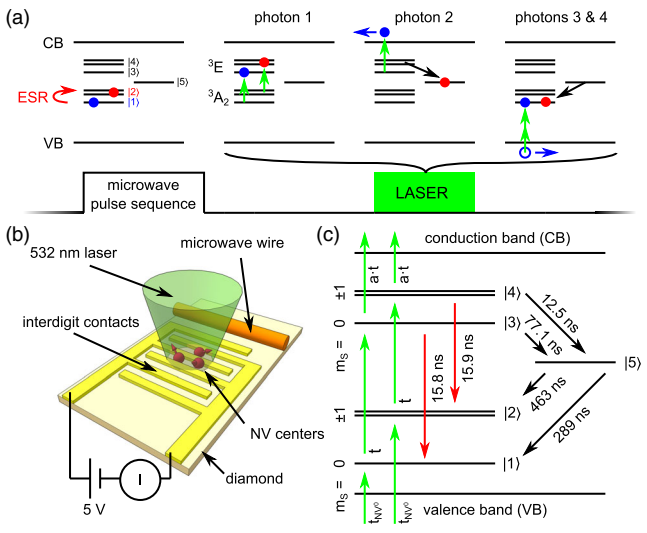

FIG. 1. (a) Spin-dependent photoionization of NV$^-$ centers used for the electrical readout of their spin states. (b) Schematic drawing of the sample and the measurement setup. (c) Level scheme used for the Monte Carlo simulation.

80-nm-thick gold layer, deposited on the diamond surface after cleaning it in a H_2SO_4 and H_2O_2 mixture and an oxygen plasma treatment. The photocurrent through the sample is measured using a transimpedance amplifier (amplification 1 GV A^{-1}, bandwidth 10 Hz). We use 5×, 10×, or 100× objectives, with numeric apertures of 0.15, 0.30, and 0.80 and ensemble sizes of 100 000, 6500, and 130 NV^- centers, respectively, estimated by comparing the diffraction-limited spot volumes of the corresponding objectives to the case of the 100× objective discussed later. The microwave with frequency ν_{MW} is delivered to the sample using a wire next to the interdigit contact structure.

We first demonstrate that coherent control can be detected electrically. To excite ESR transitions, the pulse sequence starts with a microwave pulse with power P_{MW} and varying duration T_P [top of Figs. 2(a) and 2(b)]. This initializes the spin of the NV^- $^3A_2$ ground state. After a brief delay an optical excitation pulse follows (10× objective, light power of 210 mW). Furthermore, an external magnetic field of $B_0 = 8.1$ mT is applied to the sample parallel to one of the $\{111\}$ axes via a permanent magnet so that only one crystallographic NV^- direction can be addressed. Figure 2(a) shows the pulsed electrically detected magnetic resonance (pEDMR) spectrum obtained under these conditions, monitoring the dc current through the interdigit contact structure. In contrast to previous pEDMR experiments, where the spin dependence of comparatively slow recombination or hopping processes is monitored via a boxcar integration of the current transients [15–19], the much faster pulse sequence repetition possible due to the fast photoioniziation and spin state initialization allows this vastly simpler approach. On a background photocurrent level of $I = 84$ pA resonant decreases of the photocurrent are observed at $\nu_{MW} = 2.643$ GHz and 2.818 GHz, corresponding to one $\{111\}$ orientation parallel to the B_0 field and three off-axis $\{111\}$ orientations, respectively. The resonant change of the current of $\Delta I = -1.5$ pA at 2.643 GHz corresponds to a relative spin-dependent current change (contrast) of $\Delta I/I = -1.8\%$.

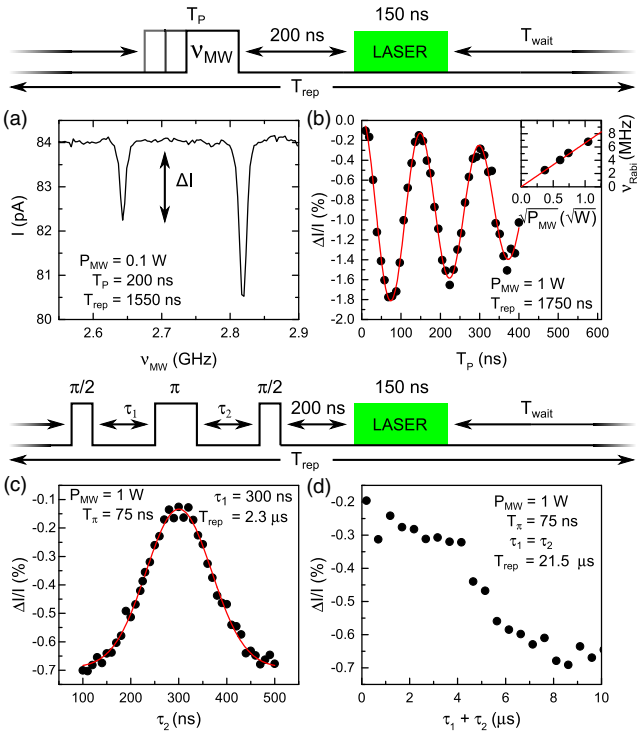

FIG. 2. (a) Pulsed electrically detected magnetic resonance spectrum for $B_0 \| \langle 111 \rangle$. Measurement time: two minutes. (b) Rabi oscillations in the contrast $\Delta I/I$ (symbols) with a fit of an exponentially decaying cosine (line). The inset shows the frequency of the Rabi oscillations (symbols) measured at different microwave powers and a linear fit (line). (c) Spin echo measurement (symbols) with a fit of a Gaussian (line). (d) Echo decay measurement showing the first ESEEM decay. The pulse sequences used for the measurements are shown on top of the respective figure. T_π is the length of a π pulse.

Rabi oscillations are observed in $\Delta I/I$ when the length T_P of the microwave pulse is changed, adjusting the waiting time T_{wait} to keep the sequence repetition time T_{rep} constant [Fig. 2(b)]. That indeed Rabi oscillations are obtained is demonstrated in the inset of Fig. 2(b), where the characteristic linear dependence of the oscillation frequency ν_{Rabi} on $\sqrt{P_{MW}}$ and, therefore, on the microwave magnetic field B_1, is observed. The Rabi oscillations exhibit an effective dephasing time of 600 ns, in accordance with other results on diamond with a neutral isotope composition [20,21]. In all experiments represented in Figs. 2(b) to 2(d) $\Delta I/I$ was determined by cycling the microwave frequency between the resonant frequency $\nu_{MW} = 2.643$ GHz and two nonresonant frequencies 2.61 GHz and 2.68 GHz [22].

The pulsed electrical detection scheme developed here allows us to detect spin echoes, e.g., by using the pulse sequence depicted on top of Figs. 2(c) and 2(d). As in the case of optically detected magnetic resonance (ODMR) [23,24] and other pEDMR [25] experiments, the corresponding Hahn echo sequence needs to be extended by a final $\pi/2$ pulse, which projects the coherence echo to a polarization accessible to electrical readout. Figure 2(c) shows the echo in $\Delta I/I$ as a function of τ_2 for a fixed τ_1. At $\tau_1 = \tau_2$ the total microwave pulse applied equals a nutation of 2π, so that the contrast is minimal, in full agreement with Fig. 2(b). For τ_2 significantly smaller or longer than τ_1, no coherence echo is formed and the final $\pi/2$ projection pulse leads to an equal distribution of spin states, which do or do not favor photoionization [25,26]. Indeed, a maximum $\Delta I/I$ of -0.7% is observed for $\tau_1 \ll \tau_2$ or $\tau_1 \gg \tau_2$, in reasonable agreement with the contrast for $\pi/2$ pulses found in the Rabi oscillation experiment.

Finally, these echo experiments can also be performed as a function of total evolution time $\tau_1 + \tau_2$ with $\tau_1 = \tau_2$, giving access, e.g., to decoherence and to weak hyperfine interaction via electron spin echo envelope modulation

(ESEEM). Figure 2(d) shows an echo decay experiment on the 2.643 GHz resonance where the decay is caused by ESEEM [27]. The experiments summarized in Fig. 2 clearly demonstrate that all fundamental coherent experiments can be performed on the NV^- center with the electrical readout scheme developed here.

We now turn to study the contrast that can be obtained by pulsed electric readout. We therefore place ourselves at $B_0 = 0$, where all four NV^- orientations merge into a single resonance at $\nu_{MW} = 2.87$ GHz, and where we can essentially flip NV^- center with all orientations into state $|2\rangle$ by a microwave π pulse. Under these conditions we study the readout contrast as a function of both the duration T_{ion} and intensity P_{ion} of the readout light pulse (Fig. 3, top), keeping the illumination as homogeneous as possible by widening the laser beam with the 5× objective [Fig. 3(a)]. For each power we find an optimum pulse length between a regime of too short pulses, where the ionization of NV^- centers mostly takes place on a time scale faster than the shelving process, and too long pulses, where mostly NV^- centers contribute to the current, which have lost their spin information by a decay through the ISC or by a preceding ionization. Optimizing P_{ion} and T_{ion} for the sample studied, we reach an optimum contrast of −14% for $P_{ion} = 100$ mW. As will be discussed below, this value is probably limited by the ionization of background substitutional nitrogen donors (N_s^0) [13,28].

The pulse powers and lengths optimal for readout may not be optimal for NV^- initialization and conversion of NV^0 to NV^- centers. Therefore in Fig. 3(b) we introduce a second laser pulse to separate the ionization from the initialization. Here, $\Delta I/I$ is plotted against the reset pulse length T_{reset} for different reset pulse powers P_{reset}. Small P_{reset} improve $\Delta I/I$ for increasing T_{reset}. The optimal $P_{reset} = 3.1$ mW leads to a maximal $\Delta I/I$ of −17%, which is reached for $T_{reset} \geq 3$ μs. For higher P_{reset} the reset pulse itself starts to ionize the NV^- centers, which decreases $\Delta I/I$.

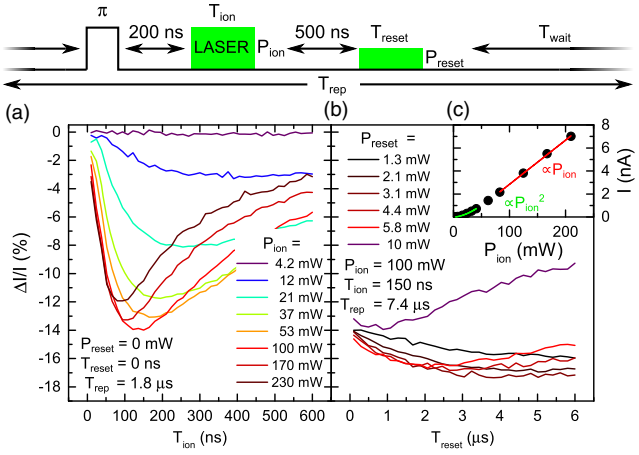

FIG. 3. (a) Contrast $\Delta I/I$ for a π microwave pulse as a function of the pulse length T_{ion} of the ionization pulse for different ionization pulse powers P_{ion}. (b) $\Delta I/I$ as a function of the pulse length T_{reset} of an additional reset pulse for different reset pulse powers P_{reset}. The pulse sequence used is shown on top of the figure. (c) Photocurrent through the sample as a function of the laser power. The green line is a fit of a polynomial of degree 2; the red line is a fit of a linear function.

We can quantitatively reproduce these observations by a Monte Carlo model of the NV^- center's optical cycle together with photoionization and recharging of the NV^0 center [Fig. 1(c)] using the partial lifetimes of Ref. [29]. The excitation time t from the $^3A_2$ ground state of the NV^- center to its ^3E excited state, the characteristic time at of the ionization process, and the lifetime of the ionized state t_{NV^0} are used as parameters in the simulation. Following Ref. [30] the photocurrent through the diamond sample is $I = eGg$ with the elemental charge e, the charge carrier generation rate G, and the photoconductive gain g. Since the charge carrier generation rate is not constant throughout the measurement we replace G by its mean $\bar{G} = (1/T_{ion}) \int_0^{T_{ion}} G(t)dt = (N/T_{ion})$ with N the number of charge carriers generated during T_{ion}. To account for a background current I_b, originating from the ionization of N_s^0, we add the generation of electrons with a rate $G_{N_s^0} = b/t$. Microwave pulse imperfections yielding a mixture between $|1\rangle$ and $|2\rangle$ at the start of the experiment are described by a parameter p multiplied with the contrast curve. The contrast then becomes

$$\frac{\Delta I}{I} = p\frac{I_{|2\rangle} - I_{|1\rangle}}{I_{|1\rangle} + I_b} = p\frac{\bar{G}_{|2\rangle} - \bar{G}_{|1\rangle}}{\bar{G}_{|1\rangle} + G_{N_s^0}} = p\frac{N_{|2\rangle} - N_{|1\rangle}}{N_{|1\rangle} + \frac{bT_{ion}}{t}}, \quad (1)$$

where the subscript $|1\rangle$ or $|2\rangle$ denotes the respective value for the initial states $|1\rangle$ and $|2\rangle$.

This term is fitted simultaneously to the data presented in Fig. 3 for the three laser powers of 53, 100, and 230 mW using the Nelder-Mead simplex algorithm. The fit parameters a, b, p, and t_{NV^0} are used globally for all fits while $t = t_{fit} \times 100\ \text{mW}/P_{ion}$ is scaled according to the laser powers P_{ion}. The turn-on-time of the AOM is simulated by linearly increasing P_{ion} during the first 50 ns of the pulse. To keep the complexity of the simulation down we use only one t_{NV^0} for all three fits, which overestimates the generated photocurrent for small laser powers and vice versa. Figure 4(a) compares $\Delta I/I$ and the fit of the Monte Carlo simulation, which are in very good agreement. We find $t_{fit} = 22$ ns, $a = 1.1$, $b = 0.19$, $p = 0.75$, and $t_{NV^0} = 10$ ns. A t in the range of tens of nanoseconds is in agreement with the onset of a saturation in the cw photocurrent at $P_{ion} = 100$ mW [cf. Fig. 3(c)], which we expect to happen at the point where the excitation time from $^3A_2$ to ^3E reaches the partial lifetime for the transition from ^3E to $^3A_2$. $p < 1$ is probably caused by the limited pulse fidelity at $B_0 = 0$, since differently oriented NV^- centers have different Rabi frequencies.

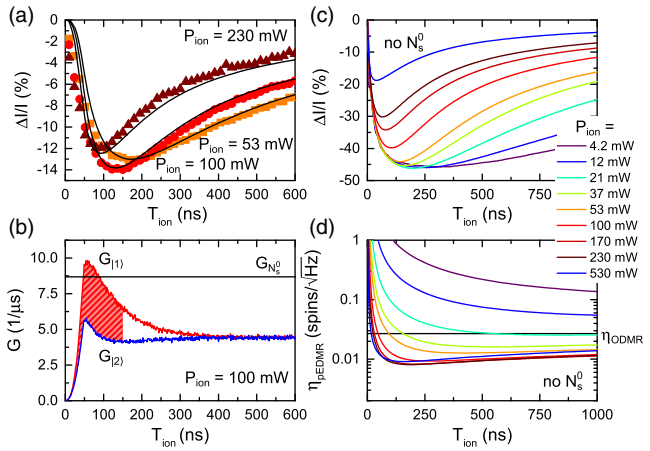

FIG. 4. (a) Contrast $\Delta I/I$ as a function of the length of the ionization pulse T_{ion} for three pulse powers taken from Fig. 3 and a simultaneous fit of a Monte Carlo simulation (black lines). (b) Simulated charge carrier generation rate $G_{|1\rangle}$ and $G_{|2\rangle}$ plotted as a function of the time during the ionization pulse T_{ion} for starting states $|1\rangle$ and $|2\rangle$, respectively. The black line depicts a constant background charge carrier generation rate $G_{\mathrm{N_s^0}}$ originating from substitutional nitrogen donors. (c) Simulated $\Delta I/I$ as function of T_{ion} for different P_{ion} under optimal conditions. (d) Sensitivity η_{pEDMR} as a function of T_{ion} for different P_{ion} under optimal conditions. η_{ODMR} marks the typical ODMR sensitivity.

The model and the parameters determined allow us to simulate the charge carrier generation dynamics in our sample during a laser pulse. Figure 4(b) shows the charge carrier generation rate $G_{|1\rangle}(t)$ and $G_{|2\rangle}(t)$ for $P_{\mathrm{ion}} = 100$ mW. The horizontal line depicts a background current originating from $\mathrm{N_s^0}$ at $G_{\mathrm{N_s^0}} = 8.6\ \mu\mathrm{s}^{-1}$. For times longer than 400 ns all spin-dependent signal is lost and the system is in a steady state with $\tilde{G}_{|1\rangle} = \tilde{G}_{|2\rangle} = 4.5\ \mu\mathrm{s}^{-1}$, each at about $1/2$ the charge carrier generation rate originating from $\mathrm{N_s^0}$. For $T_{\mathrm{ion}} = 150$ ns we find $N_{|1\rangle} = 1.0$, $N_{|2\rangle} = 0.6$, and an $\mathrm{N_s^0}$ background of 1.3 by integration over the curves, again indicating that the contrast is limited by $\mathrm{N_s^0}$ ionization.

In order to find the limits of our detection method we simulate $\Delta I/I$ without a background current, with instantaneous AOM turn-on, and with $p = 1$. Figure 4(c) plots $\Delta I/I$ simulated under these conditions versus T_{ion}. Again, $\Delta I/I$ has an optimal T_{ion} for each P_{ion}. The most notable difference is the maximal $\Delta I/I$ of -46%, which is predicted for $P_{\mathrm{ion}} = 21$ mW.

However, we expect maximum sensitivity to be obtained for rather different optical pulse conditions. A sensitivity η is usually defined by $\eta = (1/\mathrm{SNR})(N/\sqrt{\Delta f})$ with the signal-to-noise ratio SNR, the number of spins N, and the detection bandwidth Δf of the particular experiment [31]. For ODMR we find the SNR using Poissonian statistics, where the difference in photoluminescene counts $\Delta cts = cts_{|1\rangle} - cts_{|2\rangle}$ for the different initial states is divided by the shot noise generated by the number of counts $\sqrt{cts_{|1\rangle}}$ of the bright initial state $|1\rangle$. For pEDMR we use the difference in the current ΔI divided by the sum of the shot noise generated by the total current $\sqrt{2eI\Delta f}$ [32] and the amplifier input noise $\delta I_{\mathrm{amp}}\sqrt{\Delta f}$. With this we find

$$\eta_{\mathrm{ODMR}} = \frac{\sqrt{N}}{c\sqrt{cts_{\mathrm{single}}\Delta f}} = \frac{\sqrt{N}}{c\sqrt{\mathrm{rate}_{\mathrm{single}}}} \quad \text{and} \tag{2}$$

$$\eta_{\mathrm{pEDMR}} = \frac{\sqrt{2eI_{\mathrm{single}}N} + \delta I_{\mathrm{amp}}}{cI_{\mathrm{single}}}, \tag{3}$$

where the subscript single denotes the corresponding value for a single $\mathrm{NV^-}$ center, c is the contrast of the corresponding measurement, and $\mathrm{rate}_{\mathrm{single}}$ is the effective count rate of the measurement. Figure 4(d) plots the simulated sensitivity η_{pEDMR} at a sequence repetition rate of 500 kHz and for $\delta I_{\mathrm{amp}} = 0.2\ \mathrm{fA}/\sqrt{\mathrm{Hz}}$ versus T_{ion}. For each P_{ion} the sensitivity decreases (i.e., improves) with longer T_{ion} because of the increased I_{single} and c for longer T_{ion}. After reaching an optimal value η_{pEDMR} increases again since the decrease in c cancels the effects of the higher currents. The expected optimal sensitivity of $0.008\ \mathrm{spins}/\sqrt{\mathrm{Hz}}$ for pEDMR is not reached for the P_{ion} corresponding to the maximum contrast but rather for $170\ \mathrm{mW} < P_{\mathrm{ion}} < 230\ \mathrm{mW}$ and $T_{\mathrm{ion}} \approx 200$ ns. For comparison, we estimate the sensitivity for a typical ODMR experiment on a single $\mathrm{NV^-}$ center with a count rate of 100 kcounts/s and $c = 30\%$. With a typical integration time over the fluorescence of 300 ns and a shot repetition time of $1/(500\ \mathrm{kHz}) = 2000$ ns, the effective count rate becomes 15 kcounts/s. Therefore, $\eta_{\mathrm{ODMR}} = 0.027\ \mathrm{spins}/\sqrt{\mathrm{Hz}}$, which is marked by the black horizontal line in Fig. 4(d).

To put this sensitivity in absolute numbers, using a 100× objective and $P_{\mathrm{ion}} = 1.2$ mW a cw photocurrent of $I = 32$ pA is generated in our sample. Comparing the PL observed on it and on a reference sample with single $\mathrm{NV^-}$ centers allows us to estimate the number of $\mathrm{NV^-}$ centers participating to about 130 so that $I_{\mathrm{single}} = 240$ fA. Simulations under the corresponding power of 30 mW for the 5× objective predict $I_{\mathrm{single}} = 580$ fA, so that the photoconductive gain in our samples is $g = 0.35 < 1$ as expected for a metal-semiconductor-metal photodetector. Under the optimized conditions given above ($P_{\mathrm{ion}} = 170$ mW, 5× objective, 500 kHz repetition rate, $g = 0.35$, $T_{\mathrm{ion}} = 200$ ns, $I_b = 0$, $p = 1$), a single $\mathrm{NV^-}$ center should exhibit a $\Delta I = 54$ fA for $I_{\mathrm{single}} = 190$ fA, which should be easily measurable.

In summary, using a combination of pulsed photoionization and pulsed spin manipulation, we have demonstrated electrical readout of the coherent control of an ensemble of $\mathrm{NV^-}$ centers. With the help of a Monte Carlo simulation we have improved our understanding of the photoionization dynamics and find that single-spin (multishot) detection

should be feasible electrically, possibly with a higher sensitivity than optically. These results motivate a range of further studies, in particular into the relative benefits of photoconductors with ohmic or Schottky contacts and into more advanced photoionization schemes using different photon energies [28,33,34]. Furthermore, EDMR based on photoionization should be transferable to other defects and other host materials such as SiC [9–11], which might allow even easier integration of electrical spin readout, e.g., with bipolar device structures.

This work was supported financially by Deutsche Forschungsgemeinschaft via Forschergruppe 1493 (Grant No. STU 139/11-2), Priority Program 1601 (Grant No. BR 1585/8-2), and Emmy Noether Grant No. RE 3606/1-1.

*florian.hrubesch@wsi.tum.de
†friedemann.reinhard@wsi.tum.de
‡brandt@wsi.tum.de

[1] N. Bar-Gill, L. M. Pham, A. Jarmola, D. Budker, and R. L. Walsworth, Nat. Commun. **4**, 1743 (2013).
[2] A. Gruber, A. Dräbenstedt, C. Tietz, L. Fleury, J. Wrachtrup, and C. Von. Borczyskowski, Science **276**, 2012 (1997).
[3] J. M. Taylor, P. Cappellaro, L. Childress, L. Jiang, D. Budker, P. R. Hemmer, A. Yacoby, R. Walsworth, and M. D. Lukin, Nat. Phys. **4**, 810 (2008).
[4] T. Wolf, P. Neumann, K. Nakamura, H. Sumiya, T. Ohshima, J. Isoya, and J. Wrachtrup, Phys. Rev. X **5**, 041001 (2015).
[5] V. M. Acosta, E. Bauch, M. P. Ledbetter, A. Waxman, L.-S. Bouchard, and D. Budker, Phys. Rev. Lett. **104**, 070801 (2010).
[6] P. Maletinsky, S. S. Hong, M. Grinolds, B. Hausmann, M. D. Lukin, R. L. Walsworth, M. Loncar, and A. Yacoby, Nat. Nanotechnol. **7**, 320 (2012).
[7] F. Shi, Q. Zhang, P. Wang, H. Sun, J. Wang, X. Rong, M. Chen, C. Ju, F. Reinhard, H. Chen, J. Wrachtrup, J. Wang, and J. Du, Science **347**, 1135 (2015).
[8] V. R. Manfrinato, L. Zhang, D. Su, H. Duan, R. G. Hobbs, E. A. Stach, and K. K. Berggren, Nano Lett. **13**, 1555 (2013).
[9] N. R. Jungwirth, Y. Y. Pai, H. S. Chang, E. R. MacQuarrie, K. X. Nguyen, and G. D. Fuchs, J. Appl. Phys. **116**, 043509 (2014).
[10] D. J. Christle, A. L. Falk, P. Andrich, P. V. Klimov, J. U. Hassan, N. T. Son, E. Janzén, T. Ohshima, and D. D. Awschalom, Nat. Mater. **14**, 160 (2015).
[11] M. Widmann, S.-Y. Lee, T. Rendler, N. T. Son, H. Fedder, S. Paik, L.-P. Yang, N. Zhao, S. Yang, I. Booker, A. Denisenko, M. Jamali, S. A. Momenzadeh, I. Gerhardt, T. Ohshima, A. Gali, E. Janzén, and J. Wrachtrup, Nat. Mater. **14**, 164 (2015).
[12] A. Brenneis, L. Gaudreau, M. Seifert, H. Karl, M. S. Brandt, H. Huebl, J. A. Garrido, F. H. L. Koppens, and A. W. Holleitner, Nat. Nanotechnol. **10**, 135 (2015).
[13] E. Bourgeois, A. Jarmola, P. Siyushev, M. Gulka, J. Hruby, F. Jelezko, D. Budker, and M. Nesladek, Nat. Commun. **6**, 8577 (2015).
[14] P. Siyushev, H. Pinto, M. Vörös, A. Gali, F. Jelezko, and J. Wrachtrup, Phys. Rev. Lett. **110**, 167402 (2013).
[15] C. Boehme and K. Lips, Phys. Rev. B **68**, 245105 (2003).
[16] A. R. Stegner, C. Boehme, H. Huebl, M. Stutzmann, K. Lips, and M. S. Brandt, Nat. Phys. **2**, 835 (2006).
[17] W. Harneit, C. Boehme, S. Schaefer, K. Huebener, K. Fostiropoulos, and K. Lips, Phys. Rev. Lett. **98**, 216601 (2007).
[18] F. Hoehne, L. Dreher, M. Suckert, D. P. Franke, M. Stutzmann, and M. S. Brandt, Phys. Rev. B **88**, 155301 (2013).
[19] A. J. Kupijai, K. M. Behringer, F. G. Schaeble, N. E. Galfe, M. Corazza, S. A. Gevorgyan, F. C. Krebs, M. Stutzmann, and M. S. Brandt, Phys. Rev. B **92**, 245203 (2015).
[20] A. J. Parker, H.-J. Wang, Y. Li, A. Pines, and J. P. King, arXiv:1506.05484.
[21] N. Mizuochi, P. Neumann, F. Rempp, J. Beck, V. Jacques, P. Siyushev, K. Nakamura, D. J. Twitchen, H. Watanabe, S. Yamasaki, F. Jelezko, and J. Wrachtrup, Phys. Rev. B **80**, 041201 (2009).
[22] F. Hoehne, L. Dreher, J. Behrends, M. Fehr, H. Huebl, K. Lips, A. Schnegg, M. Suckert, M. Stutzmann, and M. S. Brandt, Rev. Sci. Instrum. **83**, 043907 (2012).
[23] W. G. Breiland, C. B. Harris, and A. Pines, Phys. Rev. Lett. **30**, 158 (1973).
[24] L. Childress, M. V. G. Dutt, J. M. Taylor, A. S. Zibrov, F. Jelezko, J. Wrachtrup, P. R. Hemmer, and M. D. Lukin, Science **314**, 281 (2006).
[25] H. Huebl, F. Hoehne, B. Grolik, A. R. Stegner, M. Stutzmann, and M. S. Brandt, Phys. Rev. Lett. **100**, 177602 (2008).
[26] D. P. Franke, F. Hoehne, L. S. Vlasenko, K. M. Itoh, and M. S. Brandt, Phys. Rev. B **89**, 195207 (2014).
[27] P. L. Stanwix, L. M. Pham, J. R. Maze, D. Le Sage, T. K. Yeung, P. Cappellaro, P. R. Hemmer, A. Yacoby, M. D. Lukin, and R. L. Walsworth, Phys. Rev. B **82**, 201201 (2010).
[28] E. Bourgeois, E. Londero, K. Buczak, Y. Balasubramaniam, G. Wachter, J. Stursa, K. Dobes, F. Aumayr, M. Trupke, A. Gali, and M. Nesladek, Phys. Rev. B **95**, 041402 (2017).
[29] L. Robledo, H. Bernien, T. v. d. Sar, and R. Hanson, New J. Phys. **13**, 025013 (2011).
[30] A. Rose, *Concepts in Photoconductivity and Allied Problems* (Interscience Publishers, New York, 1963).
[31] G. Boero, M. Bouterfas, C. Massin, F. Vincent, P.-A. Besse, R. S. Popovic, and A. Schweiger, Rev. Sci. Instrum. **74**, 4794 (2003).
[32] R. Müller, *Rauschen* (Springer-Verlag, Berlin, 1990).
[33] B. J. Shields, Q. P. Unterreithmeier, N. P. de Leon, H. Park, and M. D. Lukin, Phys. Rev. Lett. **114**, 136402 (2015).
[34] D. A. Hopper, R. R. Grote, A. L. Exarhos, and L. C. Bassett, arXiv:1606.06600.